Research Square

Preprints are preliminary reports that have not undergone peer review.
They should not be considered conclusive, used to inform clinical practice,
or referenced by the media as validated information.

Boosting Multifunctional Composites Thermal Conductivity via Nanometallic Interfacial Low-Frequency Phonon Resonance

Bin Wu

lwbin@ahu.edu.cn

Anhui University https://orcid.org/0000-0002-8152-4011

Qiuchen Wang

Anhui University

Ru Xia

Anhui University

Jiasheng Qian

Anhui University

Qian Li

Shanghai Jiao Tong University

Article

Keywords:

Posted Date: November 4th, 2026

DOI: https://doi.org/10.21203/rs.3.rs-11430590/v1

License: This work is licensed under a Creative Commons Attribution 4.0 International License.
Read Full License

Additional Declarations: There is **NO** Competing Interest.

Boosting Multifunctional Composites Thermal Conductivity via Nanometallic Interfacial Low-Frequency Phonon Resonance

Qiuchen Wang[1,#], Qian Li[2,#], Ru Xia[1], Jiasheng Qian[1,*], Bin Wu[1,*]

[1]Key Laboratory of Environment-Friendly Polymeric Materials of Anhui Province, School of Chemistry & Chemical Engineering, Anhui University, Hefei, Anhui, China, 230601

[2]Department of Pharmaceutical and Artificial-Intelligence Sciences, Shanghai Jiao Tong University, Shanghai, China, 200025

[#]These authors contributed equally to this work.

[*]E-mail: qianjsh@ahu.edu.cn; lwbin@ahu.edu.cn

Abstract

Modulation of inter-filler heat transfer governs the overall heat-dissipation performance of thermally conductive composites for electronics. Unlike covalent/non-covalent bond interfaces constructed using organic modifiers and inorganic secondary fillers, nanometallic bond-free interfacial structures built under mild conditions also promote interfacial thermal conduction while delivering multifunctionality. However, the related interfacial heat transfer behaviors and enhancement mechanisms remain poorly understood. Herein, guided by density functional theory and molecular dynamics simulations, we demonstrate that introducing conductive TCNQ at the graphene (Gra)-silver (Ag) interface strengthens low-frequency phonon (LFP) resonance via the resulting electron-phonon coupling (EPC) effect. Electron transfer between TCNQ and Ag optimizes the EPC effect, further activating LFP resonance across Gra and Ag surfaces to facilitate phonon transport between Gra layers. To corroborate these predictions, polybenzoxazole (PBO)

nanofibers (PNFs)-based composites ($GTAg_x$/PNFs) with TCNQ-modified graphene nanosheets (GNS)/Ag nanowires (AgNWs) composite fillers are fabricated via pressure-driven self-assembly. $GTAg_{30}$/PNFs exhibits an in-plane thermal conductivity of 28.8 W m^{-1} K^{-1} and EMI shielding effectiveness of 61.0 dB, alongside outstanding Joule heating and mechanical properties. Validated by practical cooling tests on operating electronic devices and mitigation of vehicle heat-soaking injury, this simulation-assisted low thermal resistance interface design offers a promising route toward developing high-performance multifunctional thermal management materials.

Introduction

Driven by the trend of miniaturization, dense integration, and elevated power loads in electronics, high-performance thermal dissipation acts as a decisive factor to sustain device reliability, operational performance, and cycling longevity[1]. For high-end thermal management applications, polymer-based composites merging prominent heat transfer, mechanical performances, and chemical stability represent the prevailing design route[2]. Phase mismatches between thermally conductive fillers give rise to pronounced interfacial thermal resistance (ITR), serving as one of the major obstacles to elevating the overall heat dissipation performance of composites[3]. Architectural engineering of inter-filler interfaces via covalent grafting and non-covalent assembly serves as the significant strategy to offset the ITR. Apart from constructing heat transport channels at filler interfaces using organic molecules via covalent or non-covalent bonds, the in-situ growth of inorganic secondary thermally conductive fillers also constituted as an effective approach to reduce ITR[4, 5]. Yet organic interfacial structures possessed limited thermal transport efficiency, and inorganic interfacial construction involved stringent synthetic conditions and deterioration of intrinsic heat conduction capability of primary filler, which together impeded progress of the foregoing methodologies.

Building heat transport "bridge" between fillers via configured nanoscale metallic structures with high thermal transport capability, electrical conductivity, and flexibility under mild conditions emerged as a more effective avenue. The interfacial architecture constructed by Gu et al. via in-situ grown Ag nanowires (AgNWs) between boron nitride nanosheets facilitated continuous heat transport pathways. Benefiting from the decreased ITR and boosted electrical conductivity triggered by this strategy, the composite achieved integrated multifunctional properties of efficient heat dissipation and electromagnetic interference (EMI) shielding[6]. Zhang et al additionally adopted in-situ grown Cu nanoparticles as interlayer bridges across graphene nanosheets (GNS), which effectively diminished ITR[7]. It was of great significance that microwave-triggered C-Cu heterogeneous interfaces laid a support to interpret how metallic nanoarchitectures function as heat-conducting intermedia at filler boundaries. However, the heat transfer behaviors occurring in interfacial structures have not been thoroughly revealed to date. Distinct from the heat transport mechanism within interfacial architectures linked by covalent or non-covalent bonds, Feng et al. proposed that low-frequency phonon (LFP) resonance theory offered a fresh perspective into elucidating interfacial heat transport process[8]. Carbon nanotubes redistributed LFP modes to interfacial carbon atoms, which further activated resonance with LFP of Au nanoparticles, thereby transferring more heat across the interface.

To further elucidate and harness heat transport functions of nanometal-based heterointerfaces, this work proposed a LFP resonance effect boost via electron-phonon coupling (EPC). Analysis based on density functional theory (DFT) calculations and molecular dynamics (MD) simulations revealed that the strong electron acceptor 7,7,8,8-tetracyanoquinodimethane (TCNQ) molecule facilitated interfacial charge transfer to strengthen EPC at the graphene (Gra)-silver (Ag) interface, which enhanced graphene interlayer heat transfer relying on fully developed LFP resonance. To

experimentally corroborate the simulation-derived conclusions, polybenzoxazole (PBO) nanofiber (PNFs)-matrix composites were prepared by pressure-driven self-assembly with composite fillers consisting of TCNQ-modified AgNWs (TAgNW) sandwiched between GNS (GTAgNW). The EPC effect achieved through anion-π interactions (between TCNQ and GNS) and coordination interactions (between TCNQ and AgNWs) reinforced interfacial LFP resonance, thereby yielding improved thermal conductivity performance of the composite. Benefiting from structural optimization, the resultant composited integrated prominent EMI shielding capacity, Joule heating performance, and mechanical properties. Improving interfacial thermal transport by virtue of the enhancement effect of interfacial EPC on LFP resonance provides a superior approach for designing high-performance multifunctional thermal management composites.

Results

Simulation Analysis of LFP Resonance Modulated by EPC

To thoroughly interpret the pivotal role played by TCNQ, the model structures of graphene-Ag heterostructure (GAg), TCNQ-incorporated graphene (GTG), and TCNQ-incorporated GAg (GTAg) were included in Supplementary Fig. 1 for comparative analysis. As revealed by charge-density -difference maps in Fig. 1a, e, and h, electron accumulation in GAg was mainly localized on Gra, whereas only weak electron depletion was observed on Ag, indicating limited interfacial charge transfer. For GTG and GTAg, electron accumulation and depletion regions were confined to the interfaces of TCNQ. Benefiting from Ag-N coordination interactions, the coupling degree of charge redistribution regions was enhanced, which delivered the highest interfacial charge transfer efficiency to GTAg. Quantitative Bader charge analysis further revealed a net charge transfer of 0.58 e in GTAg, confirming stronger interfacial charge transfer than in GAg and GTG (Fig. 1f)[9]. The electron localization function (ELF) maps showed more pronounced interfacial

electronic interactions in GTAg, consistent with the charge redistribution revealed by the Bader analysis (Fig. 1f i-iii). To identify the electronic states involved in interfacial charge transfer, the total and projected densities of states (TDOS/PDOS) and projected band structures were examined. GTAg exhibited pronounced overlap among the C/N p, Ag d, and Ag s/p states near the Fermi level, whereas much weaker overlap was observed in GAg and GTG (Fig. 1b–d and Supplementary Fig. 2). These results indicate stronger interfacial electronic-state hybridization in GTAg. Consistent with the projected band structures, the k-resolved orbital- and molecular state PDOS showed more pronounced and continuous contributions near the Fermi level in GTAg than in GAg and GTG, further supporting a greater degree of interfacial electronic-state hybridization in GTAg (Supplementary Figs. 3–6). From the quantitative values of graphene C p orbitals and Ag d orbitals at the band center, the energy offset of GTAg was reduced to 0.3 eV, which indicated greatly improved energy matching between C and Ag orbitals and offered favorable conditions for interfacial electron migration (Fig. 1g). To determine whether the enhanced interfacial electronic-state hybridization was accompanied by more extensive electron-phonon scattering channels, the electron and phonon linewidths of the three systems were further analyzed. GTAg exhibited a stronger electron linewidths response near the Fermi level and a broader phonon linewidths distribution than GAg and GTG, providing additional support for its stronger EPC (Supplementary Figs. 7 and 8). On this basis, the Eliashberg spectral function ($\alpha^2F(\omega)$), and the EPC constant (λ) were calculated for the three systems. As presented in Fig. 1i, the total λ (λ_T) of GTAg was extracted as 1.336 from the curves representing $\alpha^2F(\omega)$ at various frequencies. Such a value was significantly larger than 0.124 for GAg and 0.107 for GTG, revealing that EPC enhancement was realized by TCNQ-mediated reconstruction of interfacial electronic structures. Further focusing on the coupling constants in the low-frequency region below 3 THz (λ_{LF}), GTAg yielded a λ_T

occupancy of over 35%, which was far higher than those of GAg and GTG, demonstrating its superiority in the low frequency regime (Fig. 1j).

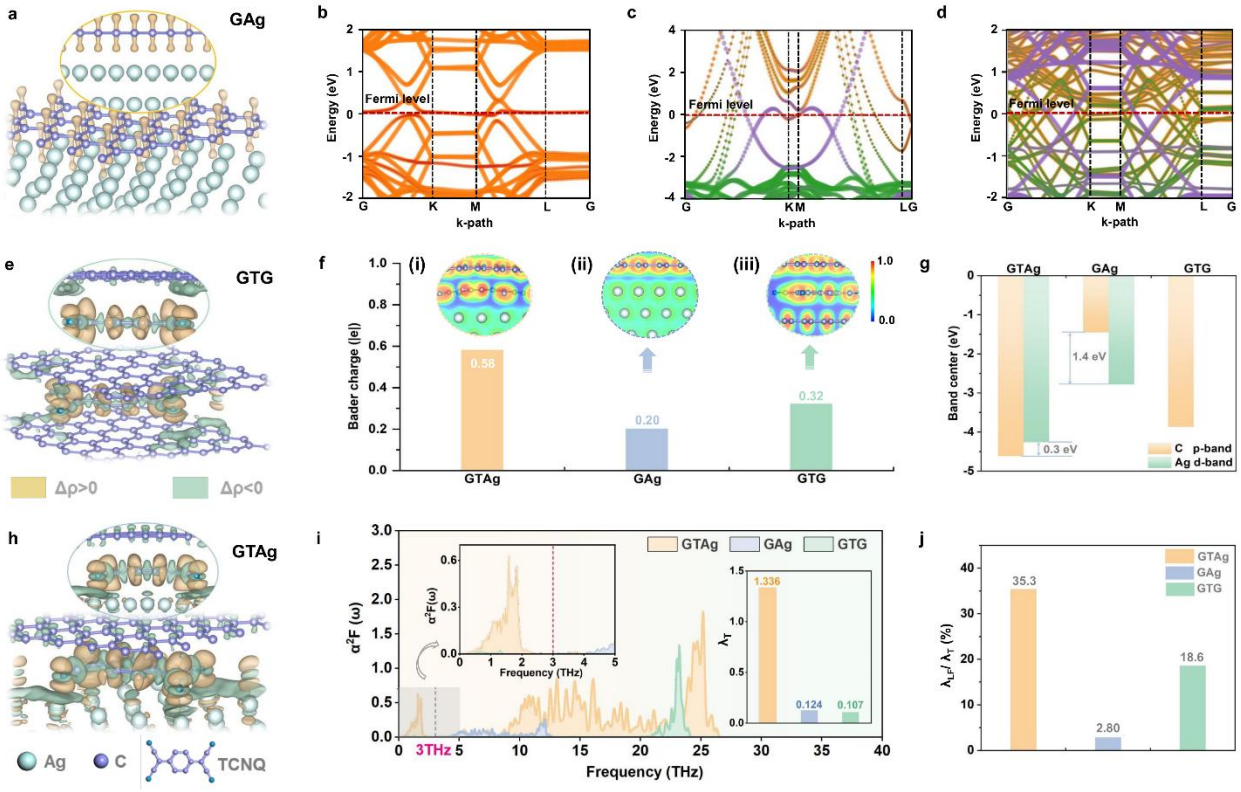


Fig. 1. TCNQ-mediated interfacial electronic reconstruction for enhanced electron–phonon coupling. Charge density difference of (a) GAg, (e) GTG, and (h) GTAg. Band structures near the Fermi energy for (b) GTG, (c) GAg, and (d) GTAg. (f) Bader charge of GTAg, GAg, and GTG, Inset: ELF at the interface of GTAg, GAg, and GTG. (g) Band-center energy values of graphene C p and Ag d orbitals in GTAg, GAg, and GTG. (i) $\alpha^2F(\omega)$ of GTAg, GAg, and GTG as a function of frequency, Inset: $\alpha^2F(\omega)$ of GTAg, GAg, and GTG below 3 THz, λ_T of GTAg, GAg, and GTG. (j) Ratio of λ_{LF} to λ_T (λ_{LF}/λ_T) in GTAg, GAg, and GTG below 3 THz.

While the foregoing analyses focus on electronic-state origins for TCNQ-tuned EPC, further insights derived from phonon density of states (PhDOS) and phonon participation ratio (PPR) illuminate that EPC facilitated LFP-mediated improvement of thermal transport across the

interface. As illustrated by PhDOS spectra across different frequencies in Fig. 2a and b, for the sub-3 THz regime conducive to long-range ordered phonon transport, GTAg achieved a low-frequency PhDOS (LF-PhDOS) contribution of 7.48%, corresponding to ~47-fold and ~34-fold enhancements relative to GAg and GTG. Consistent with the λ_{LF} results derived from electronic-state analyses, GTAg delivered more efficient thermal transport in the low-frequency region. To verify that the Ag structure serves as the primary mediator for LFP resonance-driven thermal transport enhancement within graphene interlayers, the LF-PhDOS contributions of individual components in the composite filler were calculated (Fig. 2c). Compared with the LF-PhDOS contributions from Gra and Ag in GAg and GTG, TCNQ contributed a small fraction to LF-PhDOS in GTAg, the overwhelming majority still originated from Gra and Ag. The PPR analysis further showed that GTAg exhibited a higher fraction of delocalized low-frequency phonon modes, facilitating phonon propagation across the interface and thereby enhancing interfacial heat transport. In reference to existing literature reports, PPR thresholds of $\geq$0.1 and <0.1 were attributed to delocalized phonon modes and localized phonon modes, respectively (Fig. 2d)[10, 11]. Among phonon modes < 3 THz, the fraction of low-frequency delocalized modes (LF-DM) ratio was 21.0% for GTAg, compared with 10.2% for GAg and 12.8% for GTG (Fig. 2e). Similar to the LF-PhDOS results, the delocalized low-frequency phonon modes were mainly contributed by Gra and Ag, whereas TCNQ accounted for only a minor fraction (Fig. 2f). Accordingly, TCNQ incorporation enhanced interfacial EPC and was accompanied by increased low-frequency phonon spectral weight and altered phonon localization. We propose that these changes favor LFP resonance at the Gra-Ag interface and facilitate heat transport.

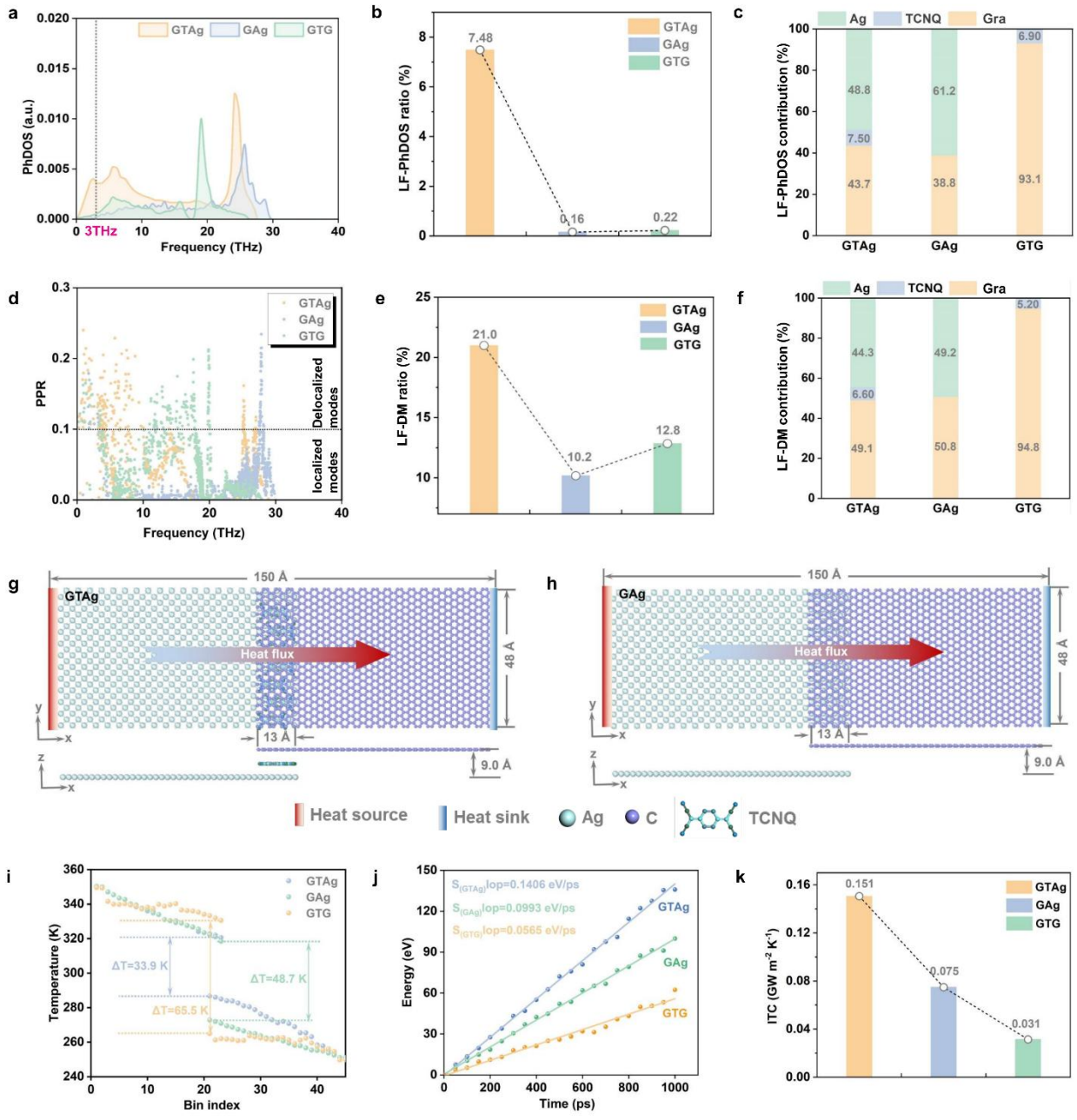


Fig. 2. Low-frequency phonon-mediated heat transport across TCNQ-modified graphene–silver interfaces. (a) Frequency-dependent PhDOS for GTAg, GAg, and GTG. (b) Fraction of the PhDOS < 3 THz. (c) Contributions of Gra, Ag, and TCNQ to the PhDOS < 3 THz. (d) PPR of GTAg, GAg, and GTG at different frequencies. (e) Fraction of delocalized modes (PPR ≥ 0.1) among all phonon modes < 3 THz. (f) Component-resolved contributions to low-frequency

delocalized modes. MD-simulated model of (g) GTAg and (h) GAg. (i) Steady-state temperature profiles, (j) Accumulated thermal energy as a function of time, and (k) ITC for GTAg, GAg, and GTG.

MD simulations provided further validation that TCNQ elevated the overall thermal conductivity of the composite filler through facilitating heat transport across the interface. For the individually built GTAg, GAg, and GTG models, heat flux was imposed along the in-plane direction of Gra (Fig. 2g, h and Supplementary Fig. 9). Heat propagated through different interfacial structures at the overlapping zone toward the top-layer Gra to realize the heat-transfer process. Upon the system achieving steady-state conditions, TCNQ gave rise to not only a smaller interfacial temperature gap (ΔT, 33.9 K) at the Gra-Ag interface than GAg, but also improved phonon-carried energy in GTAg (Fig. 2i and j). Intriguingly, despite the presence of TCNQ in GTG, LFP resonance comparable to that of the Gra-Ag interface cannot be realized between Gra, resulting in its largest ΔT and minimal phonon-carried energy. With the assistance of TCNQ, GTAg achieved an interfacial thermal conductance (ITC) far exceeding those of GAg and GTG, reaching 0.151 GW m^{-2} K^{-1} (Fig. 2k).

Preparation and Structural Characterization of $GTAg_x$/PNFs

Simulation calculations verified that TCNQ strengthened interfacial LFP resonance by modulating the EPC effect between Gra and Ag, thereby improving interfacial heat transport. PNFs matrix thermal conductive composites incorporating GTAgNW ($GTAg_x$/PNFs) were fabricated for cross-validation with simulation findings. As illustrated in Fig. 3, AgNWs obtained via the polyol method were encapsulated by TCNQ and then anchored onto the surface of electrochemically exfoliated GNS. Functioning as a favorable electron-acceptor, TCNQ accepted electrons donated by AgNWs, which enabled the formation of anion-π interactions with GNS[12]. Furthermore,

coordination interactions between the N atoms within the TCNQ and Ag^+ were utilized to construct full-fledged interfacial heat transfer channels. The subsequent pressure-assisted self-assembly process not only facilitated the oriented alignment of GTAgNW, but also endowed the $GTAg_x$/PNFs with superior practical applicability by virtue of the intrinsic properties of PNFs. Long-range ordered thermal transport pathways were further built within the composites through the final hot-pressing treatment.

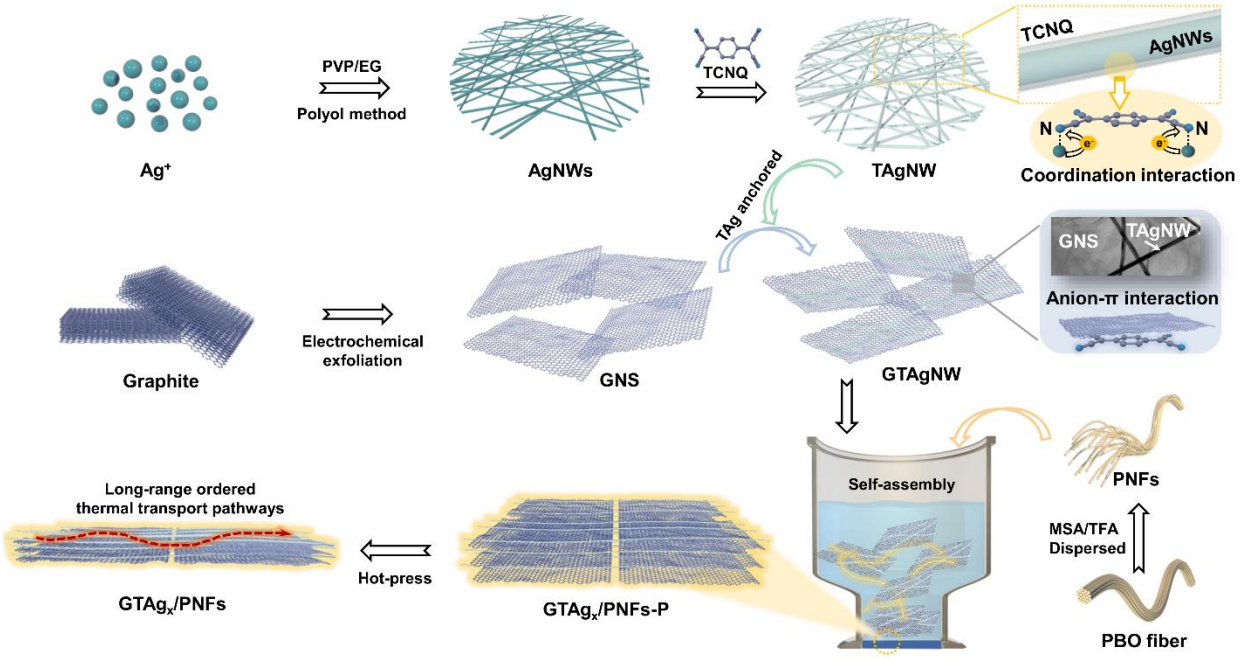
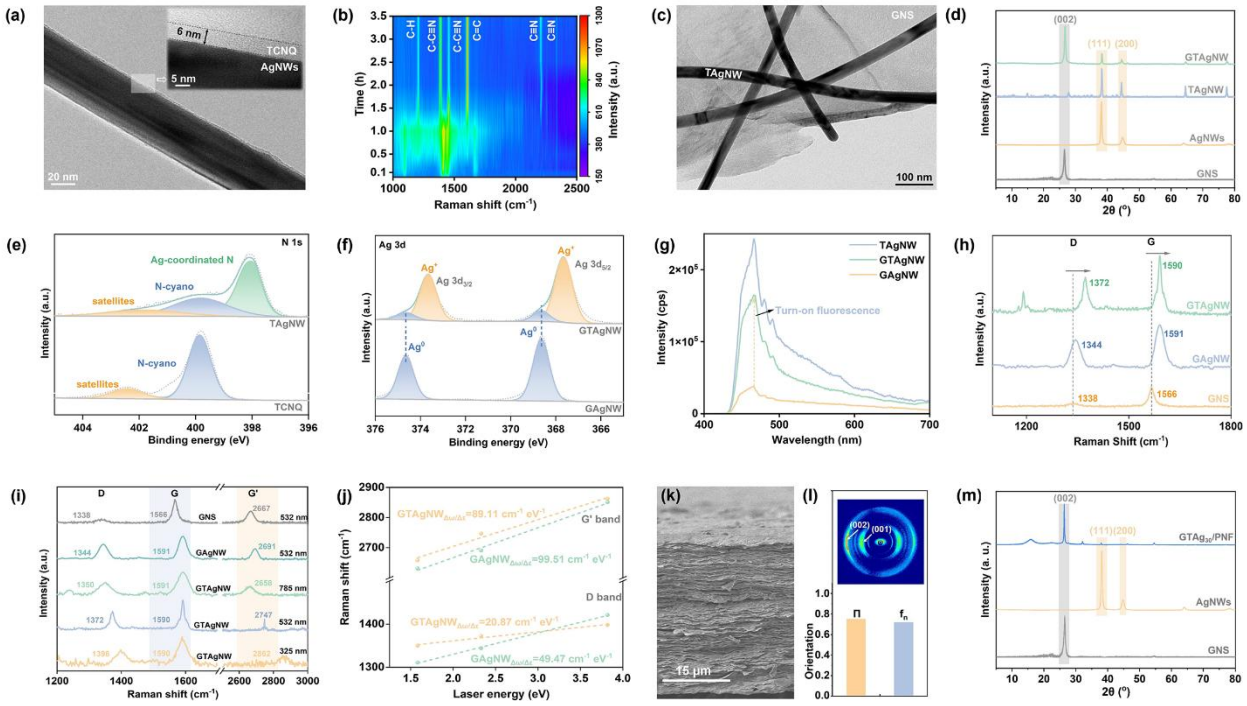


Fig. 3. Schematic illustration of the procedure for fabricating $GTAg_x$/PNFs.

Benefiting from the merits of the polyol synthetic route, AgNWs with high-aspect-ratio features were observed in Supplementary Fig. 10. The encapsulation structure of AgNWs wrapped with TCNQ was displayed in TEM, and the TCNQ layer with a thickness of around 6 nm captured by HRTEM indicated that AgNWs were efficiently modified (Fig. 4a). In-situ Raman spectra of TAgNW exhibited characteristic peaks assigned to the C-H bending, C-C≡N stretching, C=C stretching, and C≡N stretching vibrations of TCNQ, confirming the presence of TCNQ (Fig. 4b)[13]. Charge transfer between AgNWs and TCNQ reduced the vibrational energy levels, corresponding

192 to the redshift of the C-C≡N and C≡N vibrational peaks of TCNQ from 1452 cm^{-1} and 2227 cm^{-1}
193 to 1386 cm^{-1} and 2207 cm^{-1} in Raman spectra, respectively (Supplementary Fig. 11)[14]. As shown
194 in Supplementary Fig. 12, GNS synthesized by electrochemical exfoliation presented a two-
195 dimensional structure of 4.9 nm in thickness, which facilitated its heat transport performance.
196 From the TEM and SEM image of GTAgNW, it can be seen that TAgNW was firmly immobilized
197 on GNS through anion-π interactions existing between TCNQ and GNS, contributing the
198 formation of efficient interfacial structures (Fig. 4c and Supplementary Fig. 13). In the XRD
199 patterns shown in Fig. 4d, GTAgNW and TAgNW exhibit (002), (111), and (200) diffraction peaks
200 consistent with those of GNS and AgNWs, verifying the retention of structures favorable for
201 phonon and electron transport during the modification process[15]. To confirm coordination
202 interactions between TCNQ and AgNWs and anion-π interactions between TCNQ and GNS,
203 further characterizations including X-ray photoelectron spectroscopy (XPS), Fluorescence
204 spectroscopy, and Raman spectroscopy were carried out on the samples. Electron-donating Ag
205 atoms were converted into Ag^+ on the surface of AgNWs, which engaged in coordination
206 interactions with TCNQ acting as an electron acceptor[16]. Compared with the high-resolution Ag
207 3d XPS spectra of pure AgNWs, new deconvoluted peaks located at 373.3 eV and 367.3 eV
208 assigned to Ag^+ $3d_{3/2}$ and Ag^+ $3d_{5/2}$ emerged in TAgNW after electron transfer from Ag atoms
209 (Supplementary Fig. 14)[12, 14]. From Fig. 4e, distinct new deconvoluted peaks ascribed to N-Ag^+
210 coordination bonds (398.1 eV) can be observed in the high-resolution N 1s XPS spectrum of
211 TAgNW relative to pristine TCNQ, demonstrating the emergence of negatively charged TCNQ
212 ($TCNQ^-$). Discernible deconvoluted peaks ascribed to Ag^+ was still detected in the high-resolution
213 Ag 3d XPS spectra of GTAgNW, further suggesting that TCNQ incorporated in the composite
214 filler led to electron transfer, which did not occur in GAgNW (Fig. 4f). Anion-π interactions

between $TCNQ^-$ and GNS within GTAgNW served as another interfacial structure maintaining the properties of the composite filler. In Fig. 4g, $TCNQ^-$ featuring turn-on fluorescence offset partial fluorescence quenching induced by GNS upon conjugation, which yielded remarkably improved fluorescence intensity for GTAgNW relative to GAgNW[17]. Anion-π interactions also induced the blueshift of the G and D bands in the Raman spectra of GTAgNW to 1590 cm^{-1} and 1372 cm^{-1}, respectively (Fig. 4h)[18]. Compared with GNS, such a shift of the D band was more pronounced for GTAgNW than for GAgNW. Raman spectroscopy not only revealed variations in the characteristic peaks of GNS arising from non-covalent interactions; more importantly, it can directly reflect the evolution of interfacial phonon vibrational modes after modification with TAgNW[19, 20]. Compared with GNS, the G bands of both GTAgNW and GAgNW exhibited a blueshift of ≈ 25 cm^{-1} upon 532 nm excitation (Fig. 4i). The introduction of TCNQ reinforced EPC at the GNS-AgNWs interface, which yielded a more remarkable G' band blue shift up to ≈ 80 cm^{-1} in GTAgNW versus GAgNW under 532 nm excitation, provoking drastic redistribution of interfacial phonon modes and substantially boosting interfacial heat transport (Supplementary Fig. 15)[8]. To elucidate the effect originating from phonon softening, the correlation between D band and G' band frequency (ω) and excitation energy (ε) for GTAgNW and GAgNW was analyzed[21]. The dispersion slopes ($\Delta\omega/\Delta\varepsilon$) obtained at both peak positions were lower for GTAgNW compared with GAgNW, which evidenced that TCNQ-driven alterations of interfacial electronic states reinforce phonon softening and consequently intensify EPC (Fig. 4j and Supplementary Fig. 16)[22].



234

235 **Fig. 4**. **Characterization of the thermal conductive fillers and composites films.** TEM image
236 of (a) TAgNW and (c) GTAgNW. Inset: HRTEM image of TAgNW. (b) In-situ Raman spectra of
237 TAgNW. (d) XRD patterns of GNS, AgNWs, TAgNW, and GTAgNW. (e) High resolution XPS
238 spectra of N 1s for TAgNW and TCNQ. (f) High resolution XPS spectra of Ag 3d for GTAgNW
239 and GAgNW. (g) Fluorescence spectroscopy of GTAgNW, GAgNW, and TAgNW. (h) Raman
240 spectra of GTAgNW, GAgNW, and GNS. (i) Raman spectra collected for GNS, GAgNW, and
241 GTAgNW with different excitation wavelengths. (j) The frequencies of D and G' bands as
242 functions of laser energies (1.58, 2.33 and 3.82 eV correspond to 785, 532, and 325 nm,
243 respectively) for GTAgNW and GAgNW. (k) Cross-sectional SEM images of $GTAg_{30}$/PNFs. (l)
244 Π and f_h values of $GTAg_{30}$/PNFs. Inset: 2D WAXS patterns for $GTAg_{30}$/PNFs. (m) XRD patterns
245 of $GTAg_{30}$/PNFs, AgNWs, and GNS.

246 To achieve multifunctionality, GTAgNW and PNFs were composited via layer-by-layer stacking
247 using pressure-driven self-assembly. As seen from cross-sectional SEM image of the

GTAg$_{30}$/PNFs, horizontally well-aligned GTAgNW built up efficient heat transport pathways (Fig. 4k). The magnified cross-sectional SEM image of Supplementary Fig. 17 revealed that PNFs were interlaced among GTAgNW, reinforcing the functionalized structural integrity of the composite. Derived from azimuthally-integrated 2D WAXS intensity curves under X-ray incidence parallel to the (002) crystal plane, the Herman's orientation parameter (f_h) and degree of orientation (Π) further manifested the orientational behavior of GTAgNW in the GTAg$_{30}$/PNFs (Fig. 4l). Both parameters yielded orientation degrees over 0.75, corroborating the formation of efficient horizontal heat transfer pathways within the composite. XRD diffraction peaks of (002), (111), and (200) corresponding to GNS and AgNWs were detected in the GTAg$_{30}$/PNFs, indicating the well-preservation of heat conductive structures (Fig. 4m).

Thermal Conductivity (κ) and Thermal Management Performance of GTAg$_x$/PNFs, GAg$_x$/PNFs, and GTG$_x$/PNFs

The remarkable heat-transport properties imparted to GTAg$_x$/PNFs by composite fillers found full illustration in the comparison of in-plane κ ($\kappa_\parallel$) values (Fig. 5a). Consistent with the simulation results, the incorporation of TCNQ enhanced the interfacial heat transfer capability of AgNWs between GNS layers, so that the composites outperform GTG$_x$/PNFs and GAg$_x$/PNFs at different filler loadings. Owing to abundant heat transport pathways and reduced ITR, the GTAg$_{30}$/PNFs delivered a $\kappa_\parallel$ as high as 28.8 W m^{-1} K^{-1} under 30 wt% filler loading, around 2.5-fold and 1.5-fold that of GTG$_{30}$/PNFs and GAg$_{30}$/PNFs, respectively. To highlight the excellent thermal conduction performance delivered by the GTAg$_{30}$/PNFs, comparisons were made with three categories of polymer-matrix composites incorporating composite fillers with nano-metallic architectures. As illustrated in Fig. 5b, even though nano Ag functions as a favorable medium for interfacial heat transport, it delivered a lower κ value relative to the GTAg$_{30}$/PNFs. Benefiting from the role of

TCNQ, the $GTAg_{30}$/PNFs achieved a κ superior to the vast majority of reported composites, regardless of type and loading. The impact of ambient temperature upon the heat conductive property of the composites represents a key metric for examining their structural stability. The $\kappa_{\parallel}$ of the $GTAg_{30}$/PNFs upon elevated measurement temperature were illustrated in Fig. 5c. Despite the decreasing trend of $\kappa_{\parallel}$ with increasing temperature, it was maintained above 23.0 $W\ m^{-1}\ K^{-1}$, indicating great potential for a wide range of applications. The demonstration of a prolonged service lifetime for the composite is substantiated via post-thermal cycling measurements of its κ. Variations in $\kappa_{\parallel}$ of the $GTAg_{30}$/PNFs upon ten thermal cycling treatments from room temperature to 80 °C were depicted in Fig. 5d. Retention of $\kappa_{\parallel}$ values approaching 28.0 $W\ m^{-1}\ K^{-1}$ served to further confirmed the advanced heat transport architecture relative to GTG_{30}/PNFs and GAg_{30}/PNFs, and highlighted the long-term applicability of the $GTAg_{30}$/PNFs. Additional characterization of thermal contact resistance (R_c) provided evidence for the potential of the composites for thermal interface material (Fig. 5e). The $GTAg_{30}$/PNFs exhibited a minimum R_c value of 0.526 $K\ cm^2\ W^{-1}$ in comparison with PNFs, GTG_{30}/PNFs, and GAg_{30}/PNFs, which was attributed to TCNQ-assisted AgNWs that improved the interlayer heat transport capacity between GNS layers. The interfacial heat transport behavior and thermal conductivity mechanism in the composite filler was elucidated in Fig. 5f. TAgNW-derived interfacial structures between aligned GNS enabled the construction of long-range ordered heat transfer pathways. Furthermore, the LFP resonance effect occurring between TAgNW and GNS contributed to the enhancement of interfacial heat transport. Combined with the conclusions from simulations, the intrinsic electronic conductivity of TCNQ strengthened the interfacial EPC effect between GNS and AgNWs, with a concomitant improvement in their LFP resonance. The design of multi-dimensional interfacial

structures achieved a synergistic effect between EPC and LFP resonance, which efficiently boosted interfacial heat conductivity.

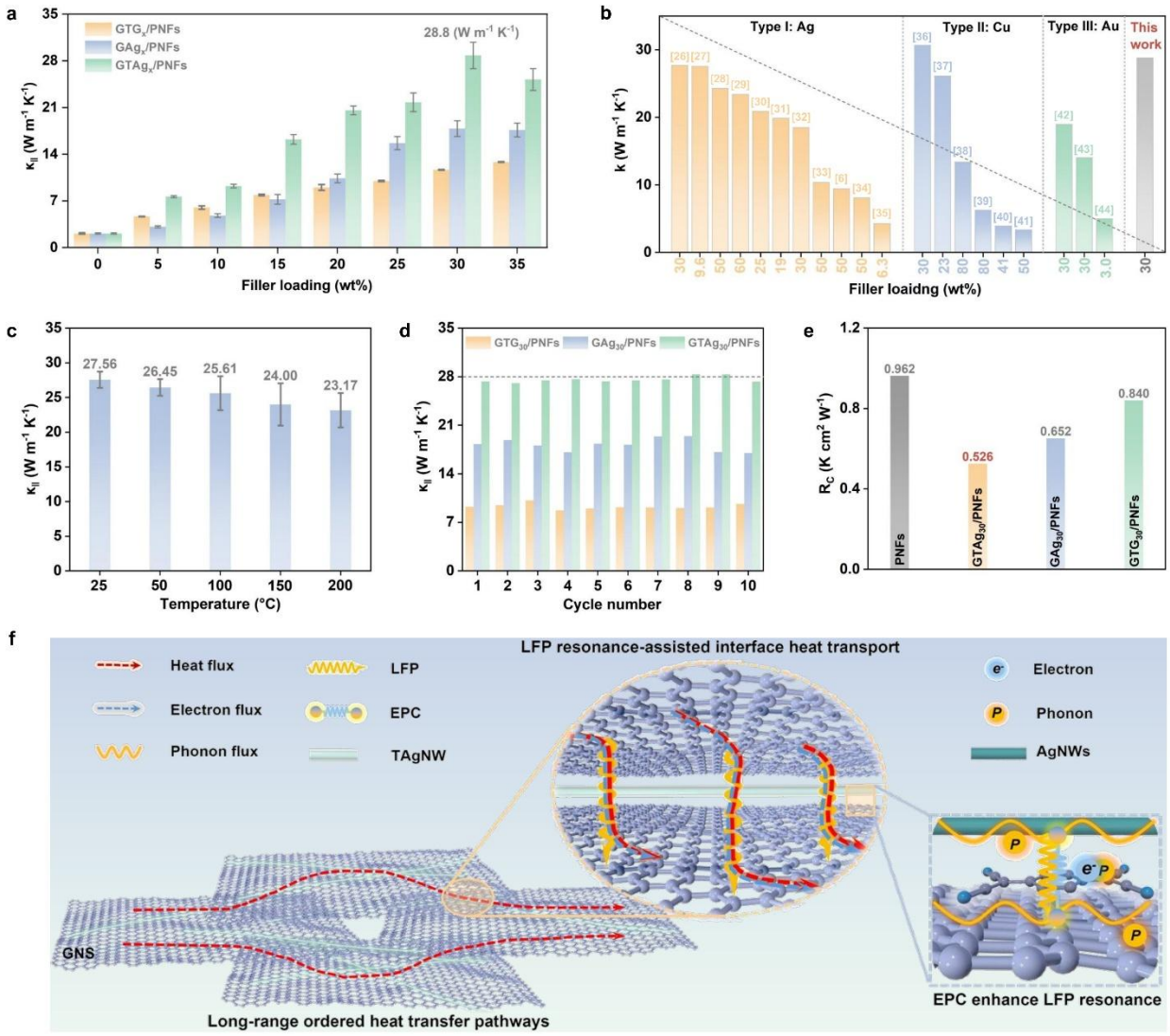


Fig. 5. Thermal transport properties of PNFs-based composites and interfacial heat transport behavior. (a) $\kappa_{\parallel}$ of GTG_x/PNFs, GAg_x/PNFs, and $GTAg_x$/PNFs with different filler loading. (b) Comparison of κ values between this work and previously reported polymer composites filled with three types of metal-containing composite fillers (Type I: Ag, Type II: Cu, and Type III: Au) [6,26–44]. (c) $\kappa_{\parallel}$ measured for the $GTAg_{30}$/PNFs at different temperatures. (d) $\kappa_{\parallel}$ of GTG_{30}/PNFs, GAg_{30}/PNFs, and $GTAg_{30}$/PNFs subjected to ten thermal cycles between room

temperature and 80 °C. (e) R_c of PNFs, GTG_{30}/PNFs, GAg_{30}/PNFs, and $GTAg_{30}$/PNFs. (f) Schematic illustration of interfacial heat transport behavior and thermal conduction mechanism for GTAgNW in composite filler.

The heat dissipation property exhibited by the composites when deployed in electronic-device systems offer a realistic assessment of its application prospects. Comparative cooling performance was carried out for $GTAg_{30}$/PNFs, GAg_{30}/PNFs, PNFs, and commercial thermal conductive pad (CTP) under operating scenarios including LED, desktop computer, and smartphone. Sandwiched between the LED and heat sink, the sample can conduct heat to bring down the surface average temperature of the LED ($T_{s\text{-}LED}$) (Supplementary Fig. 18). As revealed by the thermal infrared images in Fig. 6a and b, the LED integrated with $GTAg_{30}$/PNFs displayed a $T_{s\text{-}LED}$ around 5.2 °C lower than its GAg_{30}/PNFs counterpart, with further temperature reductions of 9.1 °C and 16.3 °C relative to CTP and PNFs after continuous lighting for 90s, respectively. After power-off, the structural advantages of the $GTAg_{30}$/PNFs enabled the $T_{s\text{-}LED}$ to drop to its minimum value more rapidly. Further evaluation of the sample's effective CPU heat dissipation performance was investigated by assembling it into a desktop computer (Supplementary Fig. 19). After 480s of CPU operation, the $GTAg_{30}$/PNFs placed between the CPU and the fan lowered the average temperature of the dashed-circle region ($T_{c\text{-}Fan}$) to 39.1°C, with a 6.4 °C reduction versus PNFs (Fig. 6d and Supplementary Fig. 20). The CPU core temperature ($T_{c\text{-}CPU}$) measured by professional testing software with the $GTAg_{30}$/PNFs installed was 19.0 °C lower than that of CTP and by as much as 28.0 °C relative to PNFs (Fig. 6e). The heat-dissipation performance of lithium-ion batteries in smartphones determines their operational stability and service life. As indicated by Supplementary Fig. 21 and Fig. 6c, the average temperature on the covered area of the lithium-ion battery ($T_{c\text{-}Li}$) with $GTAg_{30}$/PNFs attachment was not only lower than those of CTP and PNFs, but also inferior

to the temperature of its exposed area. Notably, the $T_{c\text{-}Li}$ was 5.7 ºC below that recorded for the equivalent area of the blank battery, promising prospects for smart-device applications (Fig. 6h). Solar-induced heat-soaking damage to vehicles can lead to the aging of internal electronic components and the release of harmful volatile organic compounds (VOCs). According to Fig. 6f and Supplementary Fig. 22a, the $GTAg_{30}$/PNFs was attached to model vehicle hoods and roofs made of aluminum alloy (Car 1) and carbon fiber (Car 2), respectively, to demonstrate its mitigation effect against heat-soaking damage. To comprehensively verify the heat dissipation performance, two sample free regions (i.e., hood sections A1, A2 and roof sections C1, C2) and the corresponding sample covered regions (i.e., hood sections B1, B2 and roof sections D1, D2) were defined on each vehicle. The equilibrium-temperature data acquired from the predefined regions at five specified time points during three consecutive days were summarized in Supplementary Fig. 22b and Supplementary Table 1. From the temperature-difference comparison graph illustrated in Fig. 6g, which summarized the hood- and roof-derived temperature differences of Car 1 ($\Delta T_{A1\text{-}B1}$ and $\Delta T_{C1\text{-}D1}$). It can be observed that the temperature discrepancy between sample-attached and sample-free regions was maintained at 0.9~2.9ºC at the low-temperature time points of 8:00 and 10:00, and reached 2.2~4.7ºC during the high-temperature periods at 14:00 and 16:00. On the other hand, the hood- and roof-derived temperature differences of Car 2 ($\Delta T_{A2\text{-}B2}$ and $\Delta T_{C2\text{-}D2}$) was maintained at 0.6~1.9ºC at every tested time point. The results demonstrated that the $GTAg_{30}$/PNFs delivered effective cooling performance for vehicle shells with different materials during long-term solar exposure, which served as one of the promising strategies to suppress vehicle heat-soaking damage.

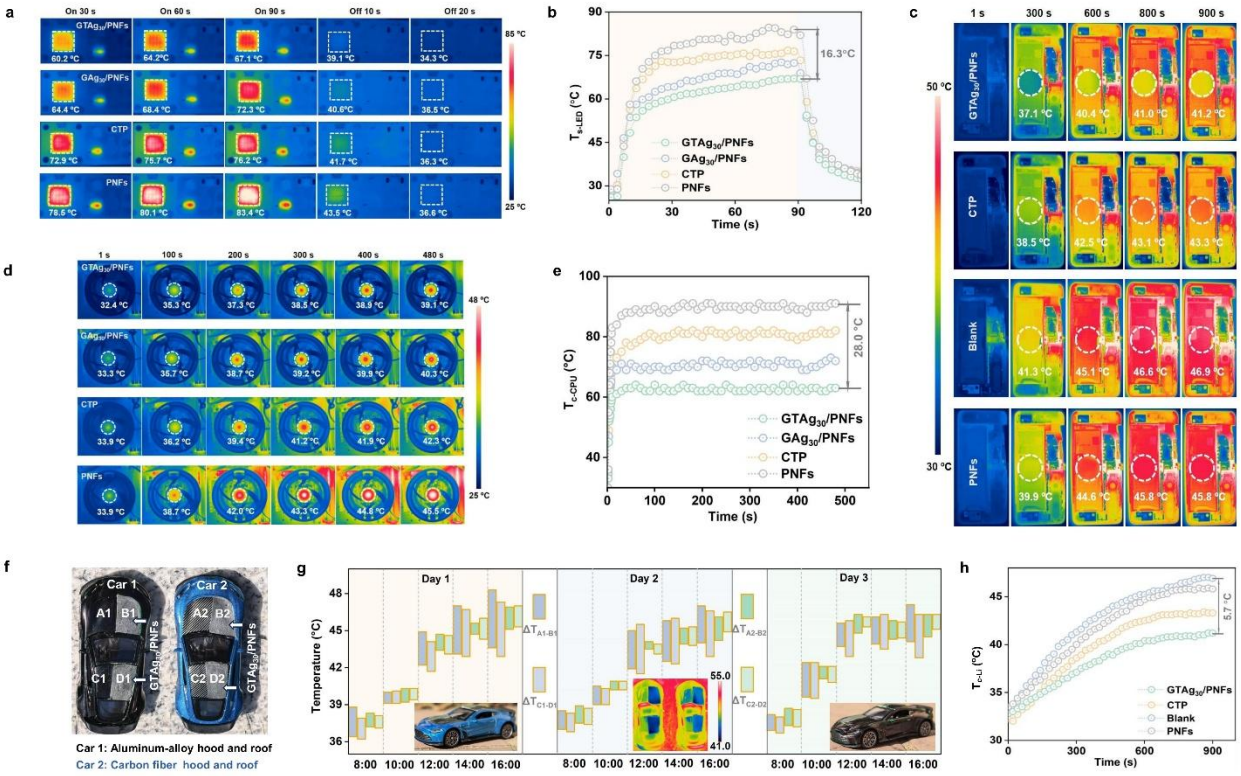


Fig. 6. $GTAg_x$/PNFs films for heat dissipation in operating electronics and solar-exposed model vehicles. (a) Thermal infrared images of LED integrated with PNFs, CTP, GAg_{30}/PNFs, and $GTAg_{30}$/PNFs and heat sink before and after power-on, respectively and (b) Corresponding $T_{s\text{-}LED}$ changes over time. (c) Thermal infrared images of the smartphone batteries in the bare state, coated with CTP, PNFs, and $GTAg_{30}$/PNFs. (d) Comparative thermal infrared images of the motherboard heat dissipation using PNFs, CTP, GAg_{30}/PNFs, and $GTAg_{30}$/PNFs and (e) $T_{c\text{-}CPU}$ evolution measured via software testing at different time points. (f) Top-view photograph of model vehicles with aluminum alloy- and carbon fiber-based hoods and roofs. Two sample-free regions and the corresponding sample-covered regions were defined on each vehicle. (g) The hood- and roof-derived temperature differences of Car 1 and Car 2. Inset: Side-view of model vehicles with aluminum alloy- and carbon fiber-based hoods and roofs and thermal infrared image. (h) The

evolution of $T_{c\text{-}Li}$ of the delineated region on the Li-ion battery as a function of operating duration. Data acquisition was performed by recording the average temperature within the white dashed box.

Electromagnetic Shielding and Joule Heating Performance

The interfacial structure optimized by TCNQ not only substantially improved the thermal management property, but also endowed the $GTAg_x$/PNFs with electrical conductivity, EMI shielding, and Joule heating performance. Conductive TCNQ accelerated the interfacial electron transfer between GNS and AgNWs, enabling the conductivity of the $GTAg_{30}$/PNFs to exceed 800 S m^{-1}, which was approximately twice that of GAg_{30}/PNFs (Fig. 7a). The EMI shielding effectiveness (SE) arises from multiple effects including EM waves reflection (SE_R) and absorption (SE_A), which are triggered by the favorable structural features of the composites[23]. The total SE (SE_T), a direct indicator for the extent of EM waves attenuation by the shielding material, equals the sum of SE_R and SE_A[24]. As presented in Fig. 7b, the $GTAg_{30}$/PNFs delivered EMI SE values exceeding 50.0 dB at frequency of 8.2~40 GHz, which were substantially higher than those of GAg_{30}/PNFs and even surpassed 61.0 dB in the Ka band. Further assessment in the Ka band showed that SE_T progressively increased as filler loading grew, peaking at 67.0 dB for 35 wt % (Fig. 7c and Supplementary Fig. 23). Meanwhile, the observed strong SE_A together with weak SE_R implied that the $GTAg_x$/PNFs avoided the risk of secondary pollution induced by the reflection of EM waves. As revealed by the power coefficients of reflection (*R*), transmission (*T*), and absorption (*A*) in Fig. 7d, the $GTAg_x$/PNFs exhibited an abrupt transition from high *T* values to high *A* and *R* values upon filler incorporation, indicating an absorption dominated EMI shielding process at low filler loadings. As the filler loading gradually increased, the layered stacking structure of the GTAgNW drove EM waves to be dissipated through more reflection processes, exhibiting a continuous rase in the *R* value. Wireless-charging experiments for a smartwatch and

lighting tests based on a Tesla coil were carried out to further evaluate the practical performance of the $GTAg_{30}$/PNFs. In contrast to PNFs, which exerted no influence on the charging process, the $GTAg_{30}$/PNFs completely interrupted the wireless-charging function when placed between the charging adapter and the smartwatch (Fig. 7e). Similarly, placing the $GTAg_{30}$/PNFs between the Tesla coil and LED inhibited the diode from lighting up, despite a 1 cm gap between them (Fig. 7f). Fig. 7g depicted the EMI shielding mechanism including absorption, reflection and multiple reflection processes of EM waves. Due to the impedance mismatch existing between the $GTAg_{30}$/PNFs and external environment, a large fraction of incident EM waves was reflected. After residual EM waves penetrated into the sample interior, both ohmic loss from conductive fillers and multiple reflection loss derived from the multilayer-oriented architecture contribute to wave attenuation.

Alongside excellent EMI shielding performance, Joule-heating functionality rendered the $GTAg_{30}$/PNFs suitable for wearable thermal textiles and electronic fabrics applications[25]. As illustrated in Fig. 7h and Supplementary Fig. 24, detailed insights into the Joule-heating behavior of the $GTAg_{30}$/PNFs were obtained by tuning the applied voltage and recording the average surface temperature within the predefined region (T_{as}). Under continuously increased voltages from 3.0 V to 8.0 V, the T_{as} reached its maximum value within 40 s and maintained for as long as 600 s. Notably, the T_{as} of 38.7 °C that fell within the comfortable temperature range for the human body was achieved under an applied voltage of 3.0 V, indicating its great suitability for warm fabrics[25]. A linear-fitting coefficient (R^2) reaching 0.96 was obtained for the relationship between the square of the applied voltage (U^2) and the T_{as}, which provided further evidence that the distinctive structure of the $GTAg_{30}$/PNFs played a dominant role in producing ohmic Joule heat (Fig. 7i). The fast-response Joule-heating behavior of the $GTAg_{30}$/PNFs was validated by performing in-situ

voltage modulation over the range of 3.0 V to 8.0 V (Fig. 7j). Stepped voltage increases drove the composite to a peak T_{as} of ~90 °C, followed by a rapid T_{as} drop upon decreasing the applied voltage. Thermochromic materials (TCM) were employed to provide a visual demonstration of the Joule-heating behavior of $GTAg_{30}$/PNFs. Supplementary Fig. 25 illustrated a three-layer-stacked architecture composed of the TCM, Anhui University logo tag (ALT), and $GTAg_{30}$/PNFs. After a voltage of 6 V was applied, the heat generated by the sample was transferred to the TCM. Upon heating, the TCM gradually turned from black to transparent, revealing the pattern of the school emblem (Fig. 7k). Such visible information disappeared progressively after removing the applied voltage. Meanwhile, thermal infrared images revealed that the average temperature inside the dashed box on the TCM first increased and then decreased during the power-on and power-off process within 90 s, further illuminating the rapid-response feature of the sample's Joule-heating performance.

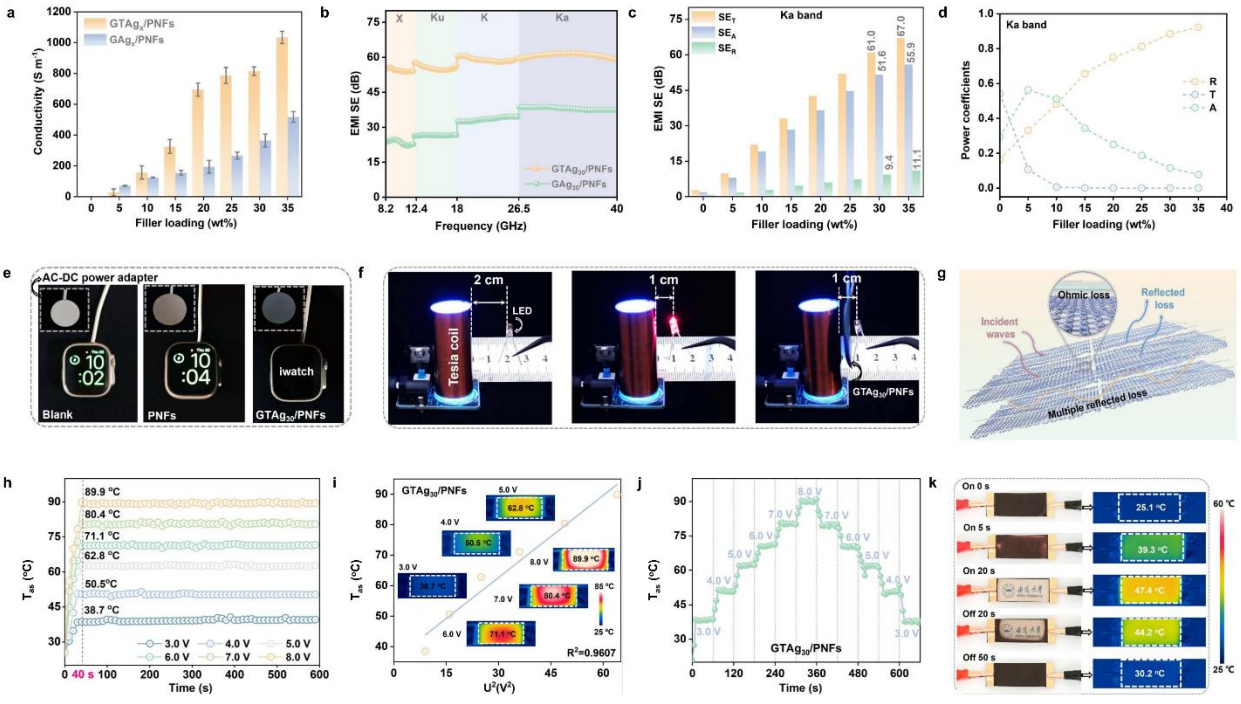


Fig. 7. $GTAg_x$/PNFs films for broadband electromagnetic shielding and voltage-controlled Joule heating. (a) Electronic conductivity of GAg_x/PNFs and $GTAg_x$/PNFs under different filler loading. (b) EMI shielding performances of GAg_{30}/PNFs and $GTAg_{30}$/PNFs across the entire frequency band. (c) SE_R, SE_A, and SE_T values and (d) Calculated EMI shielding coefficients (R, A, and T) of $GTAg_x$/PNFs with different filler loading in the Ka-band. EMI shielding performance of (e) the $GTAg_{30}$/PNFs during wireless watch-charging process and (f) the $GTAg_{30}$/PNFs before and after being put into a Tesla coil system. (g) Proposed EMI shielding mechanism of $GTAg_{30}$/PNFs. (h) Time-dependent T_{as} curves of $GTAg_{30}$/PNFs at different applied voltages. (i) Experimental data and linear fitting of T_{as} versus U^2 for $GTAg_{30}$/PNFs. Insets show thermal infrared images of $GTAg_{30}$/PNFs under varied applied voltages. (j) Change in T_{as} of $GTAg_{30}$/PNFs during voltage adjustment. (k) Visual Joule heating performances of sample constituted by TCM, ALT, and $GTAg_{30}$/PNFs at constant voltage of 6 V with varying energization durations.

Mechanical Properties and Lightweight Characteristics of $GTAg_{30}$/PNFs

Mechanical performance constitutes another important parameter for thermal management composites to achieve broad practical deployment. It can be observed from Fig. 8a that the $GTAg_{30}$/PNFs, with a dimension merely 15 mm × 7 mm, supported a maximum load of 1300 g. Such outstanding load-bearing capacity arose from the intrinsic features of the PNFs and the enhancement of interfacial interactions after TCNQ modification. It was particularly impressive that the $GTAg_{30}$/PNFs exhibited no damage even after being fabricated into vine-, snowflake- and butterfly-shaped patterns via sophisticated paper-cutting processes, and upon undergoing torsion and unidirectional folding-bending deformation (Fig. 8b and c). Even when folded into frog-, swan-, and airplane-shaped configurations, the sample can recover its original shape without sustaining damage (Fig. 8d and Supplementary Fig. 26). Composite with such mechanical

tolerance can even be placed on a dandelion without bending its pappus, demonstrating its lightweight feature (Fig. 8e). Additional tensile and bending characterizations of the $GTAg_{30}$/PNFs provided further validation for the remarkable mechanical robustness. Benefiting from TCNQ-mediated interfacial modulation, $GTAg_{30}$/PNFs delivered enhanced tensile strength (136 MPa) and elongation at break (15.3 %) compared with GAg_{30}/PNFs, outperforming pristine PNFs as well (Fig. 8f). As depicted in Fig. 8g, the corresponding Young's modulus and toughness also reached maximum values of 1.16 GPa and 11.4 MJ m^{-3}, respectively. The bending-resistance property of the $GTAg_{30}$/PNFs was investigated via 2000 consecutive cyclic bending tests on a mechanical tester (Fig. 8j and Supplementary Fig. 27). Thanks to the structural advantages, the $GTAg_{30}$/PNFs was free of distinct cracks after cyclic bending, with its tensile strength and elongation at break values retained at 114 MPa and 11.7 % (Fig. 8h). Heat flux regulation of the composite imposes requirements on the temperature-dependent effectiveness of its mechanical properties. From the results displayed in Fig. 8i, the tensile strength underwent a gradual reduction with elevated testing temperature and dropped to 68.2 MPa at 125 °C. Nevertheless, the value remained above 90 MPa at 75 °C, the normal operating temperature of electronic devices, which was sufficient to meet application requirements.

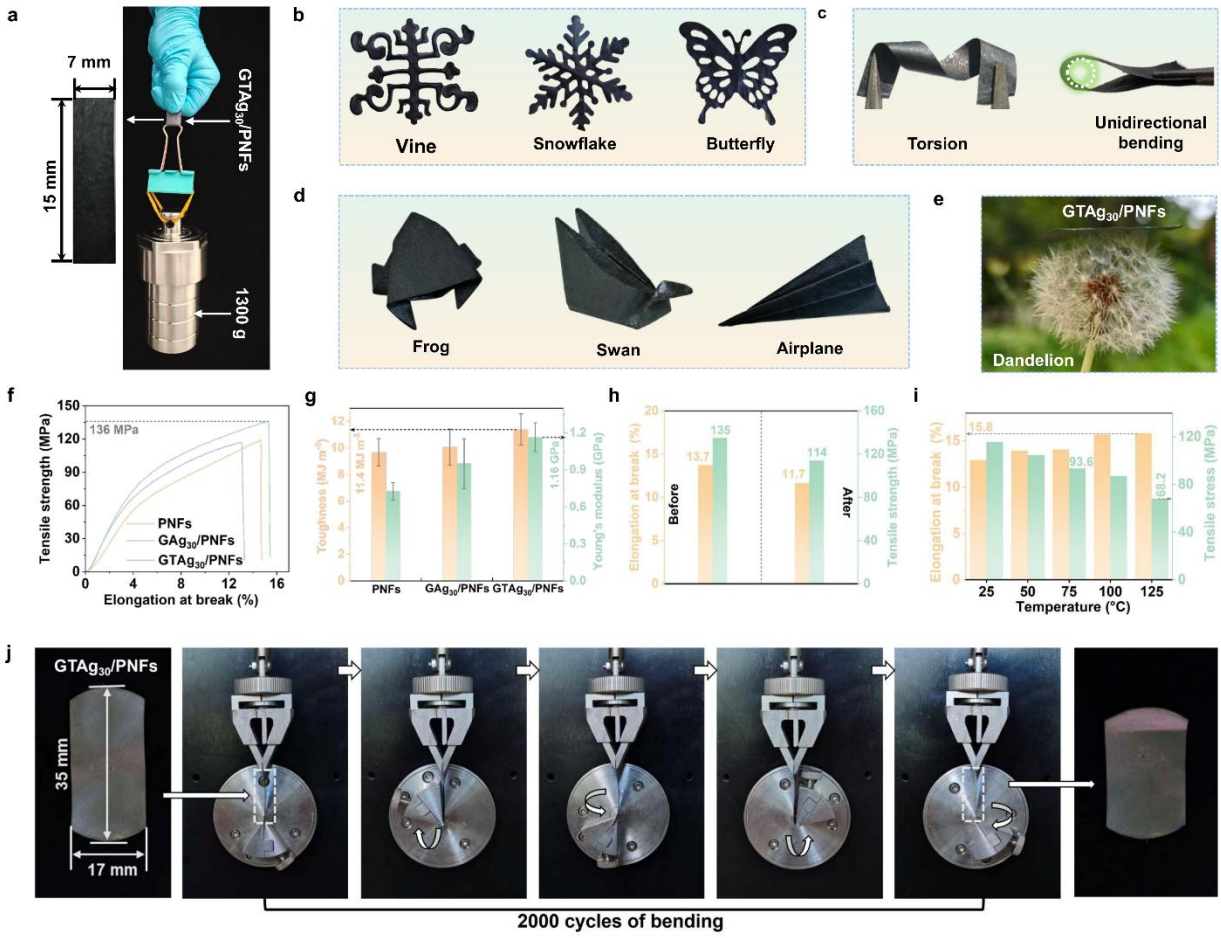


Fig. 8. Mechanical robustness of $GTAg_{30}$/PNFs films under repeated bending and elevated temperatures. (a) Photograph showing the $GTAg_{30}$/PNFs subjected to a 1300 g loading weight. (b) $GTAg_{30}$/PNFs with different patterns via paper-cutting. (c) Torsion shapes and unidirectional bending made from $GTAg_{30}$/PNFs. (d) Photograph of the $GTAg_{30}$/PNFs folded into frog-shaped, swan-shape, and airplane-shaped configurations. (e) Digital image of $GTAg_{30}$/PNFs on dandelion. (f) Tensile strength and elongation at break and (g) Toughness and Young's modulus of PNFs, GAg_{30}/PNFs, and $GTAg_{30}$/PNFs. Tensile strength and elongation at break of $GTAg_{30}$/PNFs (h) before and after 2000 cyclic bending tests and (i) across different measurement temperatures. (j) Photographs of the $GTAg_{30}$/PNFs during 2000 consecutive bending-resistance cycles.

Discussion

In summary, a unique interfacial heat transport behavior was revealed via DFT and MD simulations. The electron-transfer property of TCNQ gave rise to prominent EPC, reinforcing LFP resonance across the Gra-Ag interface and yielding a remarkable enhancement in interfacial thermal conduction. To cross-validate the simulation results, multifunctional thermally conductive PNFs-based composites containing GTAgNW were fabricated via pressure-driven self-assembly. Coupled with oriented GTAgNW alignment, the well-optimized interfacial architecture enabled the $GTAg_{30}$/PNFs to achieve an outstanding κ_l as high as 28.8 $W\ m^{-1}\ K^{-1}$. Thermal management practicability of the composites was demonstrated by evaluating its heat-dissipation performance on working LED, smartphone, and desktop computer, together with its capacity to alleviate heat-soaking damage for vehicle shell. Simultaneously, the combination of electrically conductive composite fillers and the intrinsic polymeric features of PNFs endowed the $GTAg_{30}$/PNFs with prominent EMI shielding efficiency and favorable Joule-heating, as well as superior mechanical resistance against stretching and bending deformation. Guiding the architecture construction of composites with the assistance of computational simulations delivers fresh perspectives for the rational design of multifunctional thermal-management composites.

Methods

Materials

Graphite foil (thickness: 100 μm) was purchased from Jiangsu Xianfeng Nano Materials Technology Co., Ltd., China. Silver nitrate ($AgNO_3$) was purchased from Sinopharm Chemical Reagent Co., Ltd., China. Sodium chloride (NaCl) was obtained from Shanghai Macklin Biochemical Co., Ltd., China. Ammonium sulfate ($(NH_4)_2SO_4$), acetone (C_3H_6O), anhydrous ethanol (EtOH), anhydrous acetonitrile (ACN), TCNQ, methanesulfonic acid (MSA), trifluoroacetic acid (TFA), ethyl acetate (EA), isopropanol (IPA), ethylene glycol (EG), and

polyvinylpyrrolidone (PVP) were purchased from Shanghai Aladdin Biochemical Technology Co., Ltd., China. Poly(p-phenylene-2,6-benzobisoxazole) (PBO) fibers were purchased from Toyobo Co., Ltd., Japan. Thermal grease (HT-GY260) was supplied by Shenzhen Huitianxin Technology Co., Ltd., China. κ was 4.8 W m^{-1} K^{-1}. Commercial thermal pad (CTP, Tflex HD90000) was obtained from Laird Technologies, USA. κ was 7.5 W m^{-1} K^{-1}. LED device (LY-50×24-10 W) was purchased from Shanghai Youyi Lighting Decoration Factory, China. Model vehicle was purchased from Shantou Jianfengyuan Toys Co., Ltd.

Preparation of GTAgNW

Graphite foil (2cm×2cm) and platinum foil were employed as the anode and cathode with an inter-electrode spacing kept at 2 cm, while aqueous $(NH_4)_2SO_4$ solution (0.1 mol L^{-1}) acted as the electrolyte. A constant voltage of 15 V was applied until the graphite foil was completely exfoliated. The harvested product was washed 3 times with deionized water via vacuum filtration. Subsequent freeze-drying treatment for 24 h afforded GNS.

10 mL of NaCl solution in EG (0.16 mg mL^{-1}) was injected into 10 mL of EG solution of $AgNO_3$ (51 mg mL^{-1}) at a flow rate of 1.25 mL min^{-1}. 15 mL of PVP solution in EG (70 mg mL^{-1}) was added to the above-mentioned mixture. After stirring for 20 min, the resulting sample was transferred into a polytetrafluoroethylene (PTFE)-lined autoclave and reacted at 160 °C for 5 h. The product was centrifugally washed sequentially with C_3H_6O, EtOH, and deionized water at 3000 rpm, followed by vacuum-drying at 60 °C to obtain AgNWs.

100 mL of anhydrous ACN dispersion of AgNWs (1 mg mL^{-1}) was blended with 100 mL of TCNQ anhydrous ACN solution (0.612 mg mL^{-1}), followed by stirring for 6 h at room temperature. The solid collected after filtration was washed three times with anhydrous EtOH by vacuum filtration, and then vacuum dried at 60 °C for 12 h to obtain TAgNW.

25 mL of anhydrous EtOH dispersion of TAgNW (1 mg mL^{-1}) was gradually introduced into 100 mL of GNS dispersion in anhydrous EtOH (1 mg mL^{-1}) under continuous stirring. The resulting mixture was subjected to sonication for 10 min and stirred at room temperature for 6 h. After washing with anhydrous EtOH and vacuum drying at 60 °C for 12 h, GTAgNW was obtained.

For comparison, GAgNW was prepared through the identical procedure by replacing TAgNW with AgNWs.

GNS (100 mg) was dispersed in 100 mL anhydrous ACN solution of TCNQ (2.04 mg mL^{-1}) via 10-minute sonication, and the resulting suspension was stirred at room temperature for 6 h in the dark. The harvested precipitate was washed with anhydrous ethanol, and GTGNS was collected after drying under vacuum at 60 ºC over 12 h.

Fabrication of $GTAg_x$/PNFs

PBO fibers (1.0 g) were added into a mixed solvent of MSA (50 g) and TFA (50 g) and stirred at room temperature for 72 h to obtain a PBO nanofiber sol with a concentration of approximately 1 wt %. 35 g of the above-prepared sol was diluted by adding MSA (32.5 g) and TFA (32.5 g). Under continuous stirring at 950 rpm, a mixed solution of MSA (76.6 g), EA (76.6 g), and deionized water (3.0 g) was slowly added dropwise, and the mixture was stirred for 5 min afterwards. The as-obtained gel was subjected to solvent exchange with IPA for 12 h, followed by high-speed shear dispersion at 15 000 rpm for 15 min and probe sonication at 100 W for 1 h, producing a 1 mg mL^{-1} PNFs dispersion in IPA.

A certain amount of GTAgNW was incorporated into the as-prepared PNFs/IPA dispersion (1 mg mL^{-1}) to achieve different filler concentrations of 5, 10, 15, 20, 25, 30, and 35 wt%. The resulting dispersion was subjected to 30 min of sonication followed by 24 h stirring at room

temperature. Subsequent vacuum filtration using a PTFE filter film (diameter: 0.22 μm), washing with 300 mL deionized water and hot-pressing treatment at 60 °C under 10 MPa for 2 h yielded $GTAg_x$/PNFs (x represented the mass fraction occupied by the filler during sample preparation). Following the identical fabrication procedure described above, the filler was replaced with GAgNW and GTGNS to prepare the control samples denoted as GAg_x/PNFs and GTG_x/PNFs (x stands for the mass fraction of filler added into the composite system), respectively.

All relevant details about structural characterization, performance measurements, and simulations are provided in the supporting information.

Data Availability

The authors confirm that the data supporting the findings of this study are available within the article and its supplementary information. All data are available from the corresponding author upon request.

Declaration

Ethics declaration: not applicable

References

1. Woon, W.-Y. *et al.* Thermal management materials for 3D-stacked integrated circuits. *Nat. Rev. Electr. Eng.* **2,** 598–613 (2025).
2. Xu, D., Yang, Y., Numata, K., Pang, B. Flexible polymer-based electronics for human health monitoring: a safety-level-oriented review of materials and applications. *Nano-Micro Lett.* **18,** 213 (2026).
3. Dou, Z., Lei, C., Wu, K., Yu, G. The development of thermal interface materials. *Nat. Electron.* **8,** 1146–1155 (2025).

4. Wang, R., Xu, C., Xia, R., Qian, J., Wu, B. Achieving metal-level thermal conductivity in multifunctional graphene-based composites via coordination-driven vacuum-assisted layer-by-layer self-assembly process. *Adv. Funct. Mater.* **36,** e75369 (2026).
5. Chen, J., Wang, D., Fu, J. Stiff yet tough, moisture-tolerant, room temperature self-healing and thermoconductive biomimetic nanocomposites. *Adv. Mater.* **37,** e07548 (2025).
6. Han, Y., Ruan, K., Gu, J. Multifunctional thermally conductive composite films based on fungal tree-like heterostructured silver nanowires@boron nitride nanosheets and aramid nanofibers. *Angew. Chem. Int. Ed.* **62,** e202216093 (2023).
7. Zhang, W. *et al.* Microwave-assisted fabrication of point-to-plane bridged graphene/copper hybrid fillers for high-performance thermal conductive polymer composites. *Adv. Funct. Mater.* **36,** e76199 (2026).
8. Qiu, L. *et al.* Enhancing the interfacial interaction of carbon nanotubes fibers by Au nanoparticles with improved performance of the electrical and thermal conductivity. *Carbon* **141,** 497–505 (2019).
9. Zhang, K. *et al.* Tracking regulatory mechanism of trace Fe on graphene electromagnetic wave absorption. *Nano-Micro Lett.* **16,** 66 (2024).
10. Bernges, T. *et al.* Considering the role of ion transport in diffuson-dominated thermal conductivity. *Adv. Energy Mater.* **12,** 2200717 (2022).
11. Minamitani, E., Nakamura, T., Obayashi, I., Mizuno, H. Persistent homology elucidates hierarchical structures responsible for mechanical properties in covalent amorphous solids. *Nat. Commun.* **16,** 8226 (2025).
12. Davoudi, Z. M. *et al.* Hybrid antibacterial fabrics with extremely high aspect ratio Ag/AgTCNQ nanowires. *Adv. Funct. Mater.* **24,** 1047–1053 (2014).

13. Bláha, M., Valeš, V., Bastl, Z., Kalbáč, M., Shiozawa, H. Host–guest interactions in metal–organic frameworks doped with acceptor molecules as revealed by resonance Raman spectroscopy. *J. Phys. Chem. C* **124,** 24245–24250 (2020).
14. Zhang, T. *et al.* Rationally designing high-performance versatile organic memristors through molecule-mediated ion movements. *Adv. Mater.* **35,** 2302863 (2023).
15. Tao, R. *et al.* High-conductivity–dispersibility graphene made by catalytic exfoliation of graphite for lithium-ion battery. *Adv. Funct. Mater.* **31,** 2007630 (2021).
16. Acker, D. S., Hertler, W. R. Substituted quinodimethans. I. Preparation and chemistry of 7,7,8,8-tetracyanoquinodimethan. *J. Am. Chem. Soc.* **84,** 3370–3374 (1962).
17. Iimori, T. *et al.* Effect of rigidity of microenvironment on fluorescence of 7,7,8,8-tetracyanoquinodimethane (TCNQ). *Chem. Phys. Lett.* **738,** 136912 (2020).
18. Lai, Y., Shao, H., Zhan, J. Combining computational calculations with Raman spectroscopy to identify intermolecular interactions between SCN^- and C_6F_5Br in solution. *Chem. Phys. Lett.* **746,** 137297 (2020).
19. Dresselhaus, M. S., Dresselhaus, G., Saito, R., Jorio, A. Raman spectroscopy of carbon nanotubes. *Phys. Rep.* **409,** 47–99 (2005).
20. Rao, A. M., Eklund, P. C., Bandow, S., Thess, A., Smalley, R. E. Evidence for charge transfer in doped carbon nanotube bundles from Raman scattering. *Nature* **388,** 257–259 (1997).
21. Simon, F. *et al.* Unusual Raman dispersion for D and 2D lines in high-curvature single-walled carbon nanotubes revealed by ^{13}C isotope substitution. *Phys. Rev. B* **81,** 125434 (2010).
22. Zhang, X. *et al.* Atomic-scale mechanism of enhanced electron–phonon coupling at the interface of MgB_2 thin films. *Nano Lett.* **24,** 13200–13205 (2024).

23. Yao, B. et al. Highly stretchable polymer composite with strain-enhanced electromagnetic interference shielding effectiveness. *Adv. Mater*. **32,** 1907499 (2020).
24. Fan, B. et al. Cl−-doped polypyrrole nanotubes toward robust thermal dissipation and tunable microwave absorbing/shielding properties. *Adv. Funct. Mater.* **35,** e11825 (2025).
25. Tao, D. et al. High electrical conductivity induced by surface confinement effect in heterostructured multifunctional nanofiber composite films for low-reflection electromagnetic interference shielding. *Adv. Sci.* **12,** e10386 (2025).
26. Liu, Y. *et al.* Dual conductive network enables mechanically robust polymer composites with highly electrical and thermal conductivities. *Compos. Sci. Technol.* **256,** 110777 (2024).
27. Yang, S. *et al.* Controllable Ag-rGO heterostructure for highly thermal conductivity in layer-by-layer nanocellulose hybrid films. *Chem. Eng. J.* **383,** 123072 (2020).
28. Tian, K. *et al.* Designing functional filler networks via in situ silver nanoparticles through barrier tuning and volume exclusion. *Nat. Commun.* **17,** 728 (2026).
29. Lin, D. *et al.* Polyethylene glycol modified polysiloxane and silver decorated expanded graphite composites with high thermal conductivity, EMI shielding, and leakage-free performance. *Compos. Part B Eng.* **291,** 112041 (2025).
30. Fu, C. *et al.* Improving thermal conductivity of polymer composites by reducing interfacial thermal resistance between boron nitride nanotubes. *Compos. Sci. Technol.* **165,** 322–330 (2018).
31. Yang, L. *et al.* Significant enhancement of bi-directional ultrahigh thermal conductivity in polymer composites fabricated via polyetherimide@silver core–shell structured microspheres. *Chem. Eng. J.* **500,** 156405 (2024).

32. Liu, X. *et al.* Ultrahigh thermal conductivity and photothermal conversion in interface-optimized bacterial cellulose/boron nitride nanosheets/MXene composites. *J. Mater. Sci. Technol.* **248,** 87–98 (2026).
33. Han, Y. *et al.* Highly thermally conductive aramid nanofiber composite films with synchronous visible/infrared camouflages and information encryption. *Angew. Chem. Int. Ed.* **63,** e202401538 (2024).
34. Han, Y., Ruan, K., Gu, J. Janus (BNNS/ANF)-(AgNWs/ANF) thermal conductivity composite films with superior electromagnetic interference shielding and Joule heating performances. *Nano Res.* **15,** 4747–4755 (2022).
35. Zhang, D. *et al.* Highly thermal conductive phase change composites containing Ag-welding graphene framework with excellent solar-thermal conversion and rapid heat transfer ability. *Compos. Part A Appl. Sci. Manuf.* **161,** 107128 (2022).
36. Xu, F. *et al.* A 3D interconnected Cu network supported by carbon felt skeleton for highly thermally conductive epoxy composites. *Chem. Eng. J.* **388,** 124287 (2020).
37. Yu, S. *et al.* Copper shell networks in polymer composites for efficient thermal conduction. *ACS Appl. Mater. Interfaces* **5,** 11618–11622 (2013).
38. Wang, X., Pu, Z., Yang, Y., Wei, B., Yang, S. Ultra-high thermal conductive epoxy-based copper/graphite nanoplatelets materials for heat management application. *Compos. Sci. Technol.* **224,** 109454 (2022).
39. Wang, X., Zhou, J., Yang, S. Tailoring three-dimensional copper framework in polyamide 6 for high-performance thermal management applications. *Chem. Eng. J.* **447,** 137508 (2022).
40. Zhu, W. *et al.* Carbon nanotube-Cu foam hybrid reinforcements in composite phase change materials with enhanced thermal conductivity. *Mater. Des.* **172,** 107709 (2019).

41. Vu, M. C., Bach, Q.-V., Nguyen, D. D., Tran, T. S., Goodarzi, M. 3D interconnected structure of poly(methyl methacrylate) microbeads coated with copper nanoparticles for highly thermal conductive epoxy composites. *Compos. Part B Eng.* **175,** 107105 (2019).
42. Zhang, X. *et al.* A facile method to fabricate water-dispersible hetero-structured AuNPs@BNNS hybrid filler and its application for enhancing thermal conductivity. *Compos. Commun.* **42,** 101696 (2023).
43. Yin, T. *et al.* Fabrication of heterostructured BNNS-*g*-P4VP-AuNPs hybrid fillers with uniform and dense Au nanoparticles for enhancing thermal conductivity of the nanofibrillated cellulose. *Macromol. Mater. Eng.* **307,** 2200311 (2022).
44. Balachander, N. *et al.* Nanowire-filled polymer composites with ultrahigh thermal conductivity. *Appl. Phys. Lett.* **102,** 093117 (2013).

Acknowledgements

This study was financially supported by Major scientific and technological projects of the innovation platform in Anhui Province (No. S202305a12020002) and National Natural Science Foundation of China (Grant Nos. U21A2094). Technical support for the high-performance computing platform at Anhui University.

Author Contributions

Q.W. contributed to data curation, formal analysis, investigation, and validation. Q.L. contributed resources, and R.X. contributed to methodology and supervision. J.Q. contributed to conceptualization, resource provision, supervision, and funding acquisition. B.W. contributed to conceptualization, methodology, and investigation and wrote the original draft. Q.W., Q.L., and B.W. contributed to the review and editing of the manuscript.

Competing Interests

The authors declare no conflict of interest.

Figure Legends

Fig. 1. TCNQ-mediated interfacial electronic reconstruction for enhanced electron–phonon coupling. Charge density difference of (a) GAg, (e) GTG, and (h) GTAg. Band structures near the Fermi energy for (b) GTG, (c) GAg, and (d) GTAg. (f) Bader charge of GTAg, GAg, and GTG, Inset: ELF at the interface of GTAg, GAg, and GTG. (g) Band-center energy values of graphene C p and Ag d orbitals in GTAg, GAg, and GTG. (i) $\alpha^2F(\omega)$ of GTAg, GAg, and GTG as a function of frequency, Inset: $\alpha^2F(\omega)$ of GTAg, GAg, and GTG below 3 THz, λ_T of GTAg, GAg, and GTG. (j) Ratio of λ_{LF} to λ_T (λ_{LF}/λ_T) in GTAg, GAg, and GTG below 3 THz.

Fig. 2. Low-frequency phonon-mediated heat transport across TCNQ-modified graphene–silver interfaces. (a) Frequency-dependent PhDOS for GTAg, GAg, and GTG. (b) Fraction of the PhDOS < 3 THz. (c) Contributions of Gra, Ag, and TCNQ to the PhDOS < 3 THz. (d) PPR of GTAg, GAg, and GTG at different frequencies. (e) Fraction of delocalized modes (PPR ≥ 0.1) among all phonon modes < 3 THz. (f) Component-resolved contributions to low-frequency delocalized modes. MD-simulated model of (g) GTAg and (h) GAg. (i) Steady-state temperature profiles, (j) Accumulated thermal energy as a function of time, and (k) ITC for GTAg, GAg, and GTG.

Fig. 3. Schematic illustration of the procedure for fabricating $GTAg_x$/PNFs.

Fig. 4. Characterization of the thermal conductive fillers and composites films. TEM image of (a) TAgNW and (c) GTAgNW. Inset: HRTEM image of TAgNW. (b) In-situ Raman spectra of TAgNW. (d) XRD patterns of GNS, AgNWs, TAgNW, and GTAgNW. (e) High resolution XPS spectra of N 1s for TAgNW and TCNQ. (f) High resolution XPS spectra of Ag 3d for GTAgNW

and GAgNW. (g) Fluorescence spectroscopy of GTAgNW, GAgNW, and TAgNW. (h) Raman spectra of GTAgNW, GAgNW, and GNS. (i) Raman spectra collected for GNS, GAgNW, and GTAgNW with different excitation wavelengths. (j) The frequencies of D and G' bands as functions of laser energies (1.58, 2.33 and 3.82 eV correspond to 785, 532, and 325 nm, respectively) for GTAgNW and GAgNW. (k) Cross-sectional SEM images of $GTAg_{30}$/PNFs. (l) Π and f_h values of $GTAg_{30}$/PNFs. Inset: 2D WAXS patterns for $GTAg_{30}$/PNFs. (m) XRD patterns of $GTAg_{30}$/PNFs, AgNWs, and GNS.

Fig. 5. Thermal transport properties of PNFs-based composites and interfacial heat transport behavior. (a) $\kappa_{\parallel}$ of GTG_x/PNFs, GAg_x/PNFs, and $GTAg_x$/PNFs with different filler loading. (b) Comparison of κ values between this work and previously reported polymer composites filled with three types of metal-containing composite fillers (Type I: Ag, Type II: Cu, and Type III: Au). (c) $\kappa_{\parallel}$ measured for the $GTAg_{30}$/PNFs at different temperatures. (d) $\kappa_{\parallel}$ of GTG_{30}/PNFs, GAg_{30}/PNFs, and $GTAg_{30}$/PNFs subjected to ten thermal cycles between room temperature and 80 °C. (e) R_c of PNFs, GTG_{30}/PNFs, GAg_{30}/PNFs, and $GTAg_{30}$/PNFs. (f) Schematic illustration of interfacial heat transport behavior and thermal conduction mechanism for GTAgNW in composite filler.

Fig. 6. $GTAg_x$/PNFs films for heat dissipation in operating electronics and solar-exposed model vehicles. (a) Thermal infrared images of LED integrated with PNFs, CTP, GAg_{30}/PNFs, and $GTAg_{30}$/PNFs and heat sink before and after power-on, respectively and (b) Corresponding $T_{s\text{-}LED}$ changes over time. (c) Thermal infrared images of the smartphone batteries in the bare state, coated with CTP, PNFs, and $GTAg_{30}$/PNFs. (d) Comparative thermal infrared images of the motherboard heat dissipation using PNFs, CTP, GAg_{30}/PNFs, and $GTAg_{30}$/PNFs and (e) $T_{c\text{-}CPU}$ evolution measured via software testing at different time points. (f) Top-view photograph of model

vehicles with aluminum alloy- and carbon fiber-based hoods and roofs. Two sample-free regions and the corresponding sample-covered regions were defined on each vehicle. (g) The hood- and roof-derived temperature differences of Car 1 and Car 2. Inset: Side-view of model vehicles with aluminum alloy- and carbon fiber-based hoods and roofs and thermal infrared image. (h) The evolution of $T_{c\text{-}Li}$ of the delineated region on the Li-ion battery as a function of operating duration. Data acquisition was performed by recording the average temperature within the white dashed box.

Fig. 7. GTAg$_x$/PNFs films for broadband electromagnetic shielding and voltage-controlled Joule heating. (a) Electronic conductivity of GAg$_x$/PNFs and GTAg$_x$/PNFs under different filler loading. (b) EMI shielding performances of GAg$_{30}$/PNFs and GTAg$_{30}$/PNFs across the entire frequency band. (c) SE_R, SE_A, and SE_T values and (d) Calculated EMI shielding coefficients (*R*, *A*, and *T*) of GTAg$_x$/PNFs with different filler loading in the Ka-band. EMI shielding performance of (e) the GTAg$_{30}$/PNFs during wireless watch-charging process and (f) the GTAg$_{30}$/PNFs before and after being put into a Tesla coil system. (g) Proposed EMI shielding mechanism of GTAg$_{30}$/PNFs. (h) Time-dependent T_{as} curves of GTAg$_{30}$/PNFs at different applied voltages. (i) Experimental data and linear fitting of T_{as} versus U^2 for GTAg$_{30}$/PNFs. Insets show thermal infrared images of GTAg$_{30}$/PNFs under varied applied voltages. (j) Change in T_{as} of GTAg$_{30}$/PNFs during voltage adjustment. (k) Visual Joule heating performances of sample constituted by TCM, ALT, and GTAg$_{30}$/PNFs at constant voltage of 6 V with varying energization durations.

Fig. 8. Mechanical robustness of GTAg$_{30}$/PNFs films under repeated bending and elevated temperatures. (a) Photograph showing the GTAg$_{30}$/PNFs subjected to a 1300 g loading weight. (b) GTAg$_{30}$/PNFs with different patterns via paper-cutting. (c) Torsion shapes and unidirectional bending made from GTAg$_{30}$/PNFs. (d) Photograph of the GTAg$_{30}$/PNFs folded into frog-shaped,

swan-shape, and airplane-shaped configurations. (e) Digital image of $GTAg_{30}$/PNFs on dandelion. (f) Tensile strength and elongation at break and (g) Toughness and Young's modulus of PNFs, GAg_{30}/PNFs, and $GTAg_{30}$/PNFs. Tensile strength and elongation at break of $GTAg_{30}$/PNFs (h) before and after 2000 cyclic bending tests and (i) across different measurement temperatures. (j) Photographs of the $GTAg_{30}$/PNFs during 2000 consecutive bending-resistance cycles.

Supplementary Files

This is a list of supplementary files associated with this preprint. Click to download.

- SupplementaryInformation.docx